Dual Mode Electronic Quality Factor Control of 2D Phased Array Ultrasound Transducers for Imaging and Neuromodulation

Radhakrishnan, Anand A.; Aqamolaei, Masoumeh; Costa, Tiago L.

DOI
10.1109/IUS62464.2025.11201673

Publication date
2025

Document Version
Final published version

Published in
2025 IEEE International Ultrasonics Symposium, IUS 2025

Dual Mode Electronic Quality Factor Control of 2D Phased Array Ultrasound Transducers for Imaging and Neuromodulation

1st Anand A. Radhakrishnan
Microelectronics Department
Delft University of Technology
Delft, the Netherlands
A.AlurRadhakrishnan@student.tudelft.nl

2nd Masoumeh Aqamolaei
Microelectronics Department
Delft University of Technology
Delft, the Netherlands
M.Aqamolaei@tudelft.nl

3rd Tiago L. Costa
Microelectronics Department
Delft University of Technology
Delft, the Netherlands
T.M.L.daCosta@tudelft.nl

2025 IEEE International Ultrasonics Symposium (IUS) | 979-8-3315-2332-9/25/$31.00 ©2025 IEEE | DOI: 10.1109/IUS62464.2025.11201673

***Abstract*—Ultrasound (US) technology has emerged as a powerful modality in both medical imaging and therapy, offering non-invasive, real-time, and high-resolution capabilities. Conventional dual-mode systems employ separate US transducers for imaging and therapy, each mechanically configured during fabrication for a fixed quality factor (Q-factor) through the presence of a backing layer or air-based backing layer, respectively. This approach increases system cost, physical footprint, power consumption, and integration complexity while preventing seamless real-time switching between modes. A novel electronically configurable Q-factor control circuit architecture for a single set of 2D phased-array piezoelectric transducers is proposed in this work. The proposed method employs an active damping compensation technique to electronically reduce the Q-factor during imaging mode while preserving the high-Q state for the therapeutic mode, eliminating the need for mechanical reconfiguration. System and circuit-level simulations in TSMC 180 nm BCD technology using a PZT-5A air-backed transducer BVD model demonstrate a reduction in the Q-factor from 78.3 to 8.08 with fewer than 1% variation across PVT corners. These results place the Q-factor achieved in the imaging mode within the optimal range for high-resolution ultrasound imaging, while maintaining high-Q performance for the therapeutic mode.**

***Index Terms*—Ultrasound neuromodulation, Ultrasound Imaging, Phased arrays, Quality Factor, Active Damping system**

I. Introduction

In recent years, advancements in ultrasound technology has established it as a versatile modality, enabling both non-invasive monitoring and functional stimulation of the vagus nerve, thereby improving the safety, repeatability, and accessibility of vagus nerve stimulation (VNS) therapies [1],[2]. The use of a single set of ultrasound (US) transducer array for both imaging and therapeutic applications remains challenging due to conflicting fabrication requirements. Imaging arrays employ damping backing layers to achieve low Q-factor [3]–[6], enabling short pulses and a wide bandwidth. In contrast, therapeutic arrays are typically air-backed [7], with a high Q-factor to maximize acoustic energy transfer. To tackle this issue, previous approaches frequently utilized distinct set of arrays as shown in Fig. 1a, optimized individually for imaging and therapy and operating at different frequencies and pulse durations [8], [9]. This approach increases cost, footprint, and system complexity, motivating the need for integrated dual-mode solutions.

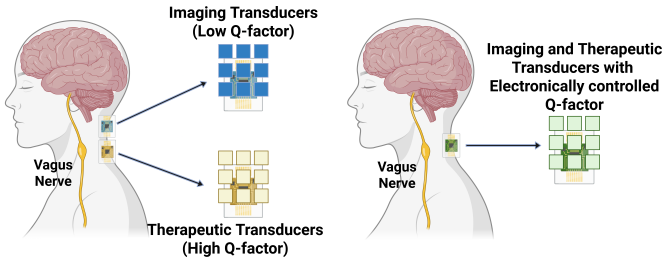

(a) (b)

Fig. 1: Imaging and Therapeutic modalities in (a) Conventional approach utilizing dedicated transducer array and custom ASIC (b) Proposed approach with electronically tunable Q-Factor with a single transducer array with custom ASIC

Previous studies on electronic active damping of piezoelectric transducers has been realized using waveform-based methods [10] or negative-feedback approaches [11]–[13]. In [10], out-of-phase damping pulses effectively cancelled residual oscillations, broadened the $-3\,\mathrm{dB}$ bandwidth, and preserved pulse amplitude; however, this required a bulky setup to generate the damping arbitrary waveform. Feedback-based damping control was showcased in [13] to ultrasound transducers, reducing the Q-factor from above 300 to below 80, thereby enabling dual-mode imaging and therapy. However, these studies rely on off-the-shelf components and single-element devices, with no CMOS implementation, limiting scalability to array-based systems where parallel Q-control is required for beamforming and neuromodulation.

This work investigates electronic control of the Q-factor in a 2-D phased-array piezoelectric transducer to enable dual-mode operation within a single array while achieving transmit beamforming. The proposed architecture, shown in Fig. 1b, integrates an $\mathrm{N} \times \mathrm{N}$ phased array with a 180-nm BCD technology application-specific integrated circuit (ASIC). The ASIC dynamically reconfigures the array: in therapeutic mode, a

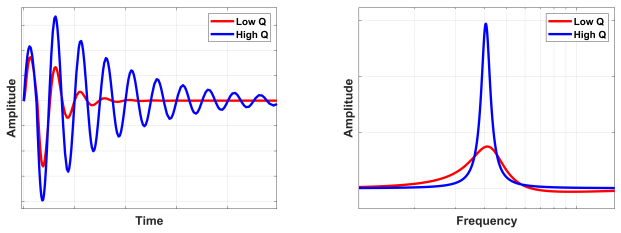

(a) (b)

Fig. 2: Q-factor response of resonant BVD model in (a) Transient domain and (b) Frequency domain

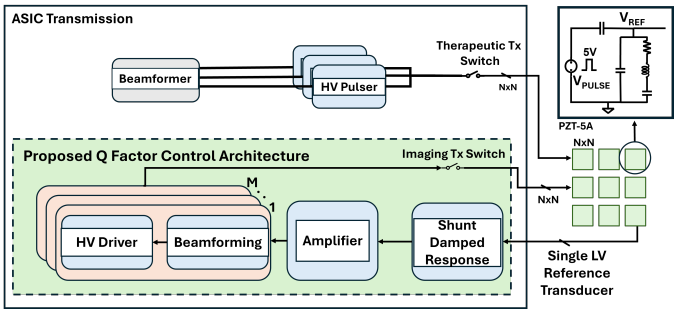

Fig. 3: Transmitter Architecture for Therapeutic and Imaging modalities

high Q-factor maximizes acoustic efficiency, while in imaging mode, the Q-factor is lowered electronically to broaden bandwidth and improve resolution. Additionally, programmable phase delays support beamforming for 2-D arrays. While conceptually proposed for ultrasound vagus nerve image-guided stimulation, the methodology is broadly applicable to any resonant transducer requiring both high and low Q-factor.

This paper is organized as follows: Section II introduces the proposed Q-factor control architecture and outlines the design requirements for damping, while Section III presents the circuit implementation and specifications. Section IV discusses the results, and Section V provides the conclusion and future perspectives

II. Proposed Q-factor Control Architecture

The Q-factor characterizes energy dissipation in US transducers, where part of the converted energy is irreversibly lost, typically as heat, and cannot be recovered [6]. The general equation for the Q-factor in resonators, such as US transducers, is defined by their frequency behaviour as in (1)

$$Q_{factor} = \frac{f_0}{BW_{3dB}} \tag{1}$$

where f_0 is the resonance frequency of the US transducer and the BW stands for the frequency bandwidth. The Q-factor quantifies the damping of an US transducer and depicts the number of oscillations sustained by an US wave before it dissipates. As shown in Fig.2, high-Q transducers exhibit prolonged high amplitude oscillations and a narrowband response, making them suitable for therapeutic applications requiring focused energy transfer. In contrast, low-Q transducers damp oscillations quickly and provide a broadband response, which is essential for diagnostic imaging.

In this work, an 8x8 PZT-5A piezoelectric transducer array with a center frequency of 4MHz and a mechanical Q-factor of 80 is is consider to simulate our approach. For effective Q-factor control, the array is assumed to have air-backed backing layer to maintain its inherent high-Q characteristics. The proposed Q-factor control circuit architecture is shown in Fig. 3. In therapeutic mode, a conventional transmit circuit is used, composed of a beamforming circuit and an HV pulser driving each of the piezoelectric transducer [14], [15] is used. However, for transmit operation during imaging mode, the system switches to the proposed Q-factor control architecture, which enables active damping along with beamforming to achieve low-Q factor for the NxN array of transducers. The proposed circuit architecture work as follows: the damped compensation signal is obtained through the shunt-damping method from a single reference transducer within the array. The amplifier generates an inverse response of the transducer's narrowband behavior, resulting in an attenuated frequency response. The damped compensation signal is extracted from the amplifier output and digitized using an ADC. The digitized response is stored once in a memory during calibration and retrieved whenever the imaging mode is triggered. This reduces power consumption while ensuring the availability of the damped response for the remaining channels within the 2D array. The optimum ADC resolution is determined via a Simulink simulation for the minimum Q-factor. The simulation setup models electronic damping of a PZT-5A transducer using a Butterworth-Van Dyke (BVD) model at 4 MHz. An ideal ADC and DAC were used to quantize and reconstruct the damped-compensation response, which was applied to evaluate Q-factor dependence on resolution. Simulations were performed for 4–11 bits, where the optimum low Q-factor was achieved between 7-11 as shown in Fig. 4. An 8-bit ADC is therefore selected, achieving a simulated Q-factor of 14.67 while minimizing area, power, and complexity. For consistency, the DAC resolution is also set to 8 bits.

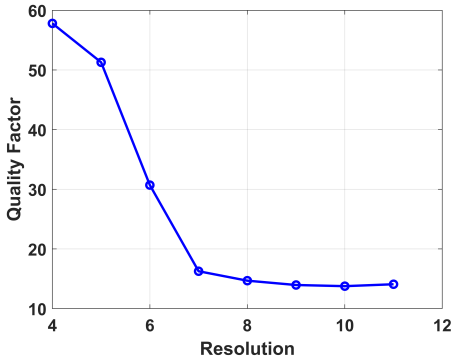

Fig. 4: Simulink simulation to determine the effect on Q-factor for different ADC resolutions

With the dampened signal stored in memory, it is used to dampen the transducer in the 2D array when transmit pulses for the imaging mode are required. In a 2D transducer array with $N \times N$ elements, mapping one beamforming/HV driver channel per element would cause an increase in area and power overhead. Instead, the channel count M is set by the maximum number of elements sharing the same phase delay, allowing one channel to drive multiple elements. In a practical implementation, a single channel can be used to drive multiple elements of the $N \times N$ array, thereby reducing the total number of required channels. As illustrated in Fig. 5a, the damped compensation signal's digital bits serve as the DAC input, digitally shifted with different phase delays ϕ_1 and ϕ_2. These are subsequently amplified and distributed to k elements through a 1:k connection scheme. In this way, each of the M channels is responsible for exciting a subset of array elements, such that the entire array of $N \times N$ elements is driven with the appropriate delays to achieve constructive interference at the focal point. Fig. 5b separately shows the corresponding damped compensation signals as transient responses, highlighting the relative delays ϕ_1 and ϕ_2. This approach ensures MN^2, significantly reducing system area and power consumption while maintaining beamforming capability. Fig. 6 shows that the minimum number of DACs and HV driver channels required by finding the maximum number of array elements sharing the same phase delay. MATLAB analysis of the 8×8 PZT-5A array across f-numbers and steering angles indicates that up to 12 channels are required at $0°$. However, since $0°$ steering is uncommon in wearable applications, this work adopts a $5°$ steering angle, reducing the requirement to 6 channels. Hence in this work, 6 channels of DAC and HV Amplifier is utilized to drive the 8x8 array. After conversion, a high-voltage linear amplifier boosts the signal to 20 V. The linear amplifier preserves signal linearity, which is critical for damping, since the waveform shape of the damped compensation response is responsible for the damping in the array.

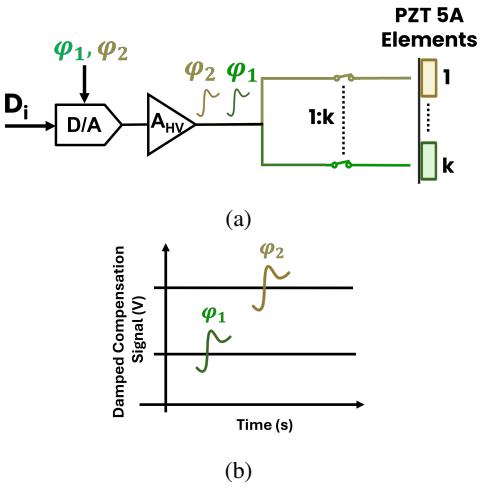

Fig. 5: (a) Channel sharing scheme with one DAC/HV driver feeding multiple PZT-5A elements. (b) Transient responses of damped compensation signals with delays ϕ_1 and ϕ_2.

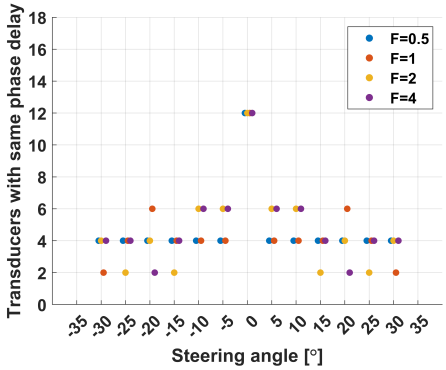

Fig. 6: Maximum number of transducers with the same phase for varying steering angles from $-30°$-$+30°$ and f-number varying from 0.5 to 4

III. Electronic Circuit Design

The proposed electronic design shown in Fig.7 integrates four key circuit blocks to realize dual-mode Q-factor control. Fig.7a shows the system level topology with different circuit blocks mentioned earlier, such as the amplifier, ADC, DACs, and HV Amplifier in order to achieve the Q-factor control of the transducers. The analog front-end is implemented using a two-stage amplifier with Miller compensation and common-mode feedback, as shown in Fig. 7b. A two-stage topology is selected to provide a wide output swing of approximately $1V_{pp}$, suitable as the input to the ADC for better linearity and quantization. In addition, this topology suppresses even-order distortion and enhances immunity to supply and substrate noise. Miller compensation is applied to separate the two poles into low- and high-frequency regions, ensuring amplifier stability. The amplifier achieves a DC gain of 61 dB and a unity-gain frequency of 127.1 MHz, as shown in Fig. 8a. A fully differential SAR ADC with top-plate sampling, a double-tail comparator, asynchronous SAR logic, and monotonic capacitor switching is employed, as illustrated in Fig. 7c. The resolution of the SAR ADC, as identified through the Simulink simulation (Fig.4), has been set at 8 bits based on these findings. Since the damped compensation signal operates at 4 MHz, a sampling frequency of 32 MHz is chosen to satisfy the Nyquist criterion and provide accurate waveform reconstruction. The ADC achieves an SNDR of 48.57 dB (ENOB $\approx$ 7.7 bits) and an SFDR of 58.21 dB, as shown in Fig. 8b. The DAC, shown in Fig. 7d, is implemented as a CDAC based on MIM capacitors. MIM devices are selected for their high capacitance density and small area, enabling faster settling to target voltage levels. The DAC is precharged to a common-mode voltage for robust operation and supports programmable digital phase delays using shift-register logic, enabling a proof-of-concept demonstration of beamforming. Its output is filtered by a first-order RC low-pass filter to suppress high-frequency artifacts. The final stage is a Class-A

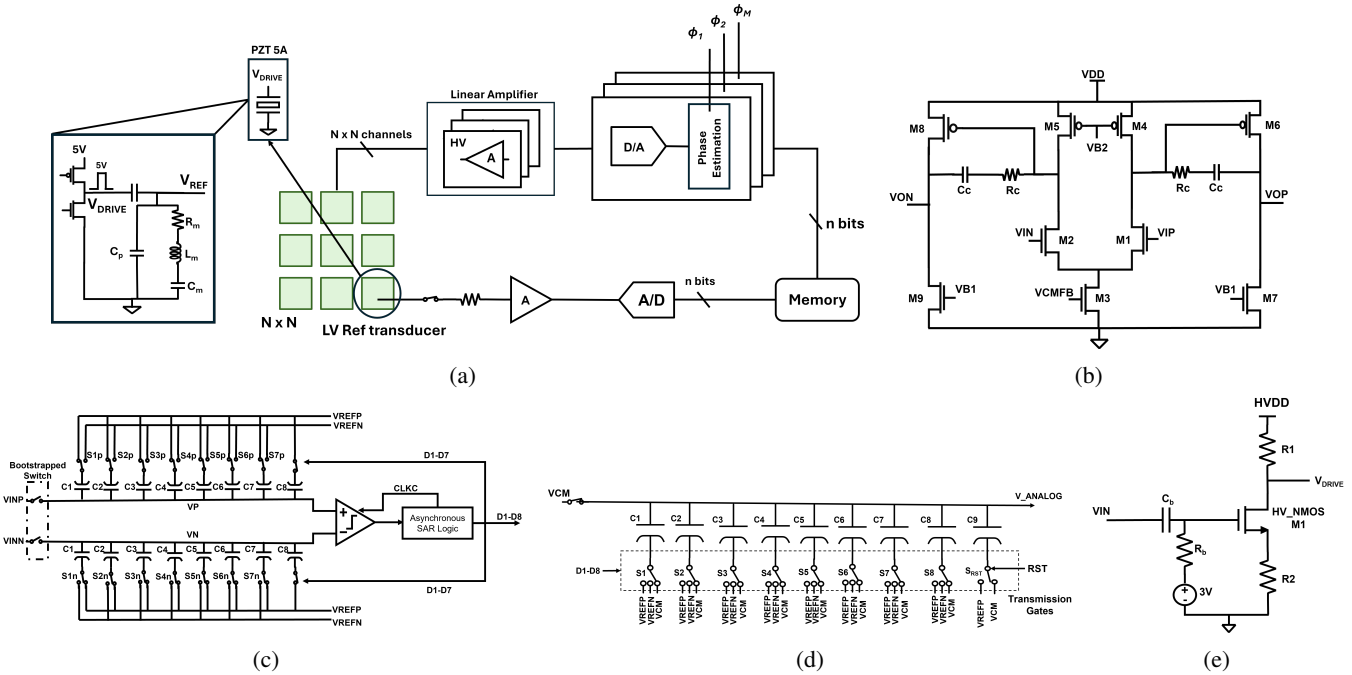

Fig. 7: Proposed Q-factor Control Architecture (a) Fully differential 2-stage Amplifier, (b) 8-bit SAR ADC, (c) 8-bit DAC with VCM Reference, and (d) HV Class A Amplifier

common-source HV NMOS amplifier with resistive degeneration, powered from a 36 V supply, as shown in Fig. 7e. This stage delivers the required 20 V_{pp} output swing for direct transducer excitation. Linearity is maintained by tuning the resistive load components (R1 and R2). The amplifier achieves a gain of approximately 21 dB, as presented in Fig. 8c.

IV. Results

This section presents the measurement and simulation results of the proposed system. First, the performance of the individual circuit blocks is validated, including the two-stage amplifier, SAR ADC, DAC, and HV linear amplifier mentioned earlier and shown in Fig.8. These results confirm that each block meets the required specifications for bandwidth, gain, resolution, and output swing. Building on these validated components, the complete Q-factor control architecture is then evaluated at the system level (Fig.7a). The most promising system-level result is shown Fig.9c, which presents the frequency-domain magnitude responses for both the undamped and electronically damped configurations. In the undamped case, the system exhibits a pronounced resonance peak corresponding to a Q-factor of 78.3. By implementing the proposed Q-factor control architecture, the Q-factor is reduced to 8.08. Since imaging-mode piezoelectric transducers typically employ a Q-factor in the range of 2 to 20, the achieved value of approximately 8.08 confirms the suitability of the proposed approach for imaging applications. This improvement is supported by transient response measurements, wherein the damped current envelope demonstrates a significantly faster decay, as illustrated in Fig.9b, compared to the sustained oscillations observed in the undamped case shown in Fig.9a. Prior to the application of the drive voltage, the signal exhibits natural oscillation and decay; however, upon applying the drive voltage after the delay, the oscillations are immediately suppressed. These observations confirm effective

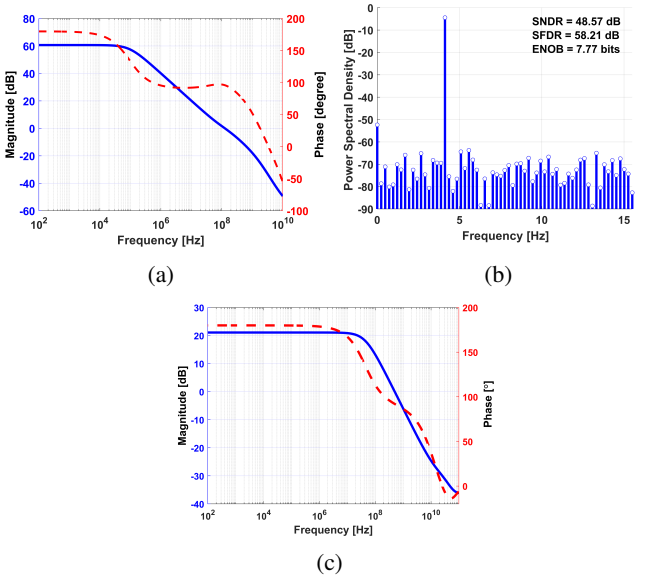

Fig. 8: Simulation results: (a) AC Gain and Phase response of Fully differential Amplifier (b) Power Spectral Density of the ADC showcasing an SNDR of 48.57dB, and (c) AC Gain and Phase response of HV Linear Amplifier.

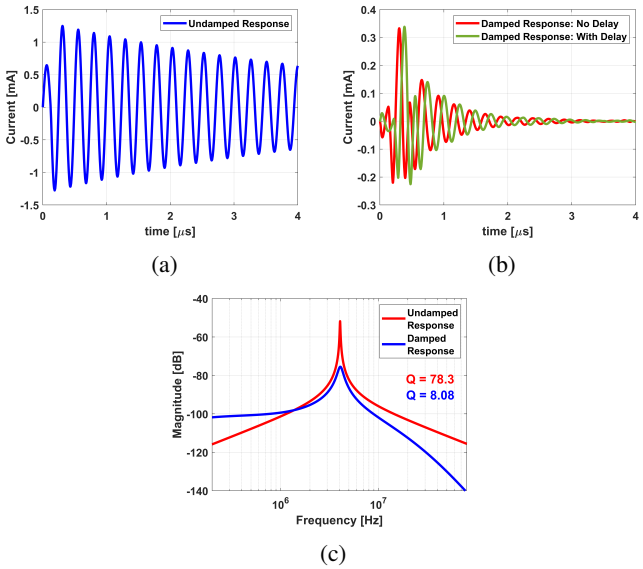

Fig. 9: Simulation results: (a) Undamped Current Response, (b) Damped Current Response with and without delay, and (c) Frequency Response and Q-factor comparison.

energy dissipation and suppression of resonance.

Furthermore, Process, Voltage and Temperature (PVT) corner analysis was conducted to evaluate the robustness of the proposed architecture, for power supply voltages of 1.8 V nominal and temperatures of 20 °C, 27 °C, and 45 °C. Under nominal conditions, the Q-factor was 8.077, while cross all PVT corners, the Q-factor ranged from a minimum of 8.072 to a maximum of 8.129, corresponding to a total variation of approximately 0.7%. This minimal deviation demonstrates that the shunt-damping network maintains stable performance despite variations in fabrication process, supply voltage, and operating temperature. The complete system, including both low-voltage and HV subsystems, consumes 191.3 mW, which is relatively high for wearable ultrasound applications. This power corresponds to one fully differential amplifier, one SAR ADC, one DAC, and one HV amplifier. The amplifier and ADC serve only as a calibration circuit and are used once to store the damped compensation signal, thereby reducing their impact on continuous power consumption. The dominant contribution arises from the HV amplifier alone, consuming 182.3 mW from a 36 V supply. When this is coupled to 6 channels of DAC and HV Amplifier to drive the 8x8 array elements, the total power consumption is estimated to be much higher. Future work should focus on optimizing the DAC and HV amplifier design to reduce overall system power. Even though no circuit layout was yet implemented, the total estimated area of the system, integrating the proposed Q-factor architecture with an amplifier, 8-bit SAR ADC, six channels of DAC and HV amplifiers, is approximately $0.77\text{mm} \times 1\text{mm}$.

V. Conclusion

This work presented a novel electronically configurable Q-factor control architecture for 2D phased-array piezoelectric ultrasound transducers, enabling dual-mode operation for imaging and therapy within a single system. Simulated in TSMC 180-nm BCD process, the design employs active damping to reduce the transducer Q-factor from 78.3 to 8.08, achieving the bandwidth required for imaging while preserving high-Q therapeutic capability. The architecture supports phased-array beamforming and shows less than 1% variation across PVT corners, confirming robust operation. However, the total power consumption of 191.3 mW is high for wearable applications, and calibration memory remains off-chip.

Future work will focus on lowering power consumption, integrating on-chip memory, and embedding dedicated beamforming circuits for real-time imaging. Complete layout and post-layout verification will be required to evaluate parasitic effects, while hardware prototyping and in vitro/in vivo testing will be essential to validate performance and demonstrate clinical suitability.

References

[1] J. Blackmore, S. Shrivastava, J. Sallet, C. R. Butler, and R. O. Cleveland, "Ultrasound neuromodulation: A review of results, mechanisms and safety," *Ultrasound in medicine & biology*, vol. 45, no. 7, pp. 1509–1536, 2019.

[2] M. E. Downs, S. A. Lee, G. Yang, S. Kim, Q. Wang, and E. E. Konofagou, "Non-invasive peripheral nerve stimulation via focused ultrasound in vivo," *Physics in Medicine & Biology*, vol. 63, no. 3, p. 035 011, 2018.

[3] J. Li, Y. Ma, T. Zhang, K. K. Shung, and B. Zhu, "Recent advancements in ultrasound transducer: From material strategies to biomedical applications," *BME Frontiers*, vol. 2022, p. 9 764 501, 2022.

[4] X. Bai, D. Wang, L. Zhen, *et al.*, "Design and micromanufacturing technologies of focused piezoelectric ultrasound transducers for biomedical applications," *International Journal of Extreme Manufacturing*, vol. 6, no. 6, p. 062 001, 2024.

[5] M. Postema, *Fundamentals of medical ultrasonics*. CRC Press, 2011.

[6] H. Bhugra and G. Piazza, *Piezoelectric MEMS resonators*. Springer, 2017.

[7] H. S. Gougheri, A. Dangi, S.-R. Kothapalli, and M. Kiani, "A comprehensive study of ultrasound transducer characteristics in microscopic ultrasound neuromodulation," *IEEE Transactions on Biomedical Circuits and Systems*, vol. 13, no. 5, pp. 835–847, 2019.

[8] V. Pashaei, P. Dehghanzadeh, G. Enwia, M. Bayat, S. J. A. Majerus, and S. Mandal, "Flexible body-conformal ultrasound patches for image-guided neuromodulation," *IEEE Transactions on Biomedical Circuits and Systems*, vol. 14, no. 2, pp. 305–318, 2020.

[9] V. Pashaei, A. Roman, and S. Mandal, "Conformal ultrasound transducer array for image-guided neural therapy," in *2018 IEEE Biomedical Circuits and Systems Conference (BioCAS)*, 2018, pp. 1–4.

[10] J. Yen and Z. Nussbaum, "Active damping of air-backed ultrasonic transducers using arbitrary waveform generators," in *2020 IEEE International Ultrasonics Symposium (IUS)*, IEEE, 2020, pp. 1–4.

[11] Nguyen and Howe, "Quality factor control for micromechanical resonators," in *1992 International Technical Digest on Electron Devices Meeting*, IEEE, 1992, pp. 505–508.

[12] A. Humphris, J. Tamayo, and M. Miles, "Active quality factor control in liquids for force spectroscopy," *Langmuir*, vol. 16, no. 21, pp. 7891–7894, 2000.

[13] C.-M. Chen and B. Choubey, "Ultrasound transducer quality factor control using coupled external electrical resonator," in *2018 IEEE SENSORS*, IEEE, 2018, pp. 1–4.

[14] H. Rivandi and T. L. Costa, "A 2d ultrasound phased-array transmitter asic for high-frequency us stimulation and powering," *IEEE transactions on biomedical circuits and systems*, vol. 17, no. 4, pp. 701–712, 2023.

[15] T. Costa, C. Shi, K. Tien, J. Elloian, F. A. Cardoso, and K. L. Shepard, "An integrated 2d ultrasound phased array transmitter in cmos with pixel pitch-matched beamforming," *IEEE Transactions on Biomedical Circuits and Systems*, vol. 15, no. 4, pp. 731–742, 2021.